Electronic Supplementary Information

S-Doped Defective Pd{111} Facets Endow Au@AuPd Nanowire Networks with Superior Electrocatalytic Performance for Alkaline ORR

Hao Ding,[a] Jiayi Hou,[a] Mengjiao Hao,[a] Xiaoying Xu,[a] and Haibing Xia[a,*]

[a] State Key Laboratory of Crystal Materials, Shandong University, Jinan, 250100, P. R. China.

*E-mail: hbxia@sdu.edu.cn

Experimental Section

Materials. Chloroauric acid tetrahydrate ($HAuCl_4 \cdot 4H_2O$, 99%), trisodium citrate dihydrate ($Na_3C_6H_5O_7 \cdot 2H_2O$, 99%) and sodium borohydride ($NaBH_4$, 99%) were purchased from Sinopharm Chemical Reagent Co., Ltd. (Shanghai, China). Reduced glutathione (GSH, 98%) was purchased from Aladdin (Shanghai, China). Sodium tetrachloropalladate (II) hydrate (Na_2PdCl_4, 99%), commercial Pt/C catalysts (nominally 20% on carbon black) and commercial Pd/C catalysts were purchased from Alfa Aesar (Tianjin, China). All the chemicals were used as received without further treatment. All the experiments used Milli-Q water with a resistivity of 18.2 MΩ cm.

The aqua regia (3:1 v/v HCl (37%): HNO_3 (65%) solutions) was used for cleaning all glassware thoroughly. And all glassware was washed completely with Milli-Q water before use. (Caution! Aqua regia are dangerous and must be used with extreme care; never store these solutions in closed containers.)

Characterizations

JEOL JEM-2100F transmission electron microscope was used to characterize the morphology of the samples. Transmission electron microscope (TEM) images and high-resolution transmission electron microscope (HR-TEM) images of the samples were obtained at the acceleration voltage of 200 KV. High-angle annular dark-field-scanning transmission electron microscopy (HAADF-STEM) and HAADF-STEM-EDS mapping images were also acquired by a JEOL JEM-2100F transmission electron microscope with a STEM unit.

X-ray diffraction (XRD) patterns were obtained on a PANalytical X'pert3 powder diffractometer (40 kV, 40 mA) using a Cu Kα radiation (λ=0.15418 nm) and was recorded in the range from 20° to 90° (2θ) with a step length of 0.08°.

Raman spectra were recorded by a Renishaw inVia Reflex Raman spectrometer with a 633 nm laser at room temperature.

X-ray Photoelectron Spectroscopy (XPS) spectra were recorded by Thermo Fisher Scientific ESCALAB 250 XPS spectrometer with a monochromatic Al Kα X-ray radiation.

CO stripping measurement.

Prior to CO stripping measurements, a 0.5 M H_2SO_4 electrolyte was deoxygenated by bubbling with ultra-high purity N_2 for at least 30 min, followed by bubbling with ultra-high purity CO for 30 min to facilitate CO adsorption. Next, the electrode potential was then held at 0.03 V (vs. Ag/AgCl) in the CO-saturated electrolyte for 1000 s to achieve CO monolayer coverage under continuous CO bubbling. Then, residual CO was rigorously purged from the

electrolyte by bubbling with ultra-high purity N_2 for 30 min to ensure complete CO removal. Finally, two consecutive cyclic voltammograms (CVs) were recorded from -0.2 to 1.2 V (vs. Ag/AgCl) at a scan rate of 50 mV s^{-1}.

Electrochemical measurements.

Electrochemical measurements for ORR were conducted using a CHI 660D electrochemical workstation at room temperature in a standard three-electrode cell, which comprised a saturated calomel electrode (SCE, double-junction) as the reference electrode, a Pt wire as the counter electrode, and a glassy carbon rotating disk electrode (GC-RDE, 5-mm diameter, geometric area = 0.19625 cm^2) as the working electrode. All potentials in this work were converted to the reversible hydrogen electrode (RHE) scale using the equation: $E_{RHE}=E_{SCE} + 0.0591 \times pH + 0.241$.

Prior to ORR measurements, the RDE surface was sequentially polished with 0.05-μm alumina slurry, ultrasonically cleaned in Milli-Q water and ethanol, and then dried at room temperature. Typically, the working electrode—an RDE modified with the $S_{4.9}$-doped $Au_{89.3}@Au_{1.3}Pd_{5.8}/S^{B3.8A1.1}$ NWNs—was prepared as follows. 30 μL of the catalyst ink, containing homogeneously dispersed $S_{4.9}$-doped $Au_{89.3}@Au_{1.3}Pd_{5.8}/S^{B3.8A1.1}$ NWNs, was drop-casted onto the bare GC-RDE surface. After drying at room temperature, 15 μL of 0.2 wt% Nafion/ethanol solution was further covered onto the catalyst layer, followed by subsequent drying. The total Pd mass loading was set as 16 μg_{Pd} cm^{-2}.

For comparison, an RDE modified with commercial Pt/C catalysts was prepared as follows. The catalyst ink containing commercial Pt/C was obtained by dispersing 1.23 mg of commercial Pt/C in 1 mL of Milli-Q water containing 50 μL of Nafion solution (5 wt%) under ultrasonication for 30 min. 20 μL of the resulting catalyst ink was drop-casted onto the bare GC-RDE surface, followed by drying at room temperature. The Pt mass loading was controlled at 25 μg_{Pt} cm^{-2}.

ORR measurements.

Cyclic voltammetry (CV) was performed in N_2-saturated 0.1 M KOH electrolyte from 0 to 1.6 V vs. RHE at a scan rate of 100 mV s^{-1}.

Linear sweep voltammetry (LSV) was carried out in both N_2 and O_2-saturated 0.1 M KOH electrolyte at a scan rate of 10 mV s^{-1} and different ration speeds ranging from 400 to 2025 rpm.

Accelerated durability tests (ADTs) employed potential cycling between 0.6 and 1.1 V vs. RHE (100 mV s^{-1}) in O_2-saturated KOH for 10000 cycles.

Fig. S1 LSV curves (A) and histogram (B) of half-wave potentials ($E_{1/2}$) of four types of Au@AuPd NWNs (a to d), which were prepared under different concentrations of Pd^{2+} precursor: 0.080 mM (a), 0.096 mM (b), 0.120 mM (c), and 0.160 mM (d).

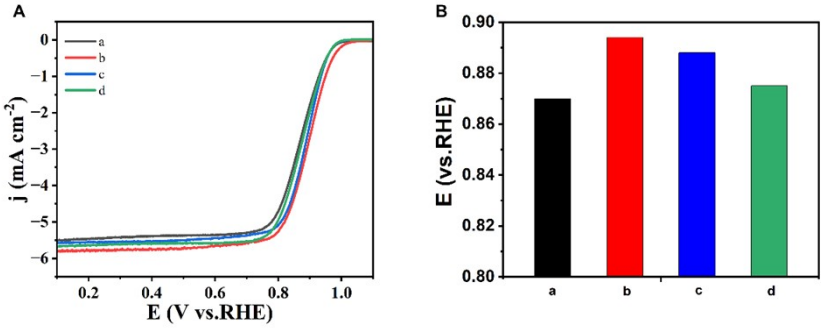

In our work, both the ratio of Pd atoms and the ratio of S^{2-} to S_2^{2-} species on the surfaces of the $S_{4.9}$-doped $Au_{89.3}@Au_{1.3}Pd_{5.8}/S^{B3.8A1.1}$ NWNs are crucial for enhancing their performance. Therefore, to select the optimal concentration of Pd^{2+} precursor for the $S_{4.9}$-doped $Au_{89.3}@Au_{1.3}Pd_{5.8}/S^{B3.8A1.1}$ NWNs, four types of Au@AuPd NWNs were firstly prepared and evaluated by their LSV curves (**Fig. S1A**) and determined by their corresponding $E_{1/2}$ values (**Fig. S1B**). It is clearly seen that the $E_{1/2}$ values of these four types of Au@AuPd NWNs are 0.870 V, 0.894 V, 0.888 V and 0.875 V, respectively. Therefore, the optimal Pd^{2+} concentration for synthesis of Au@AuPd NWNs is 0.096 mM.

Fig. S2 LSV curves (A) and histograms (B) of half-wave potentials ($E_{1/2}$) of four types of S-doped Au@AuPd NWNs (a to d), which were prepared under different concentrations of GSH precursor: 0.080 mM (a), 0.096 mM (b), 0.120 mM (c), and 0.160 mM (d). The concentration of the Pd^{2+} precursor is 0.096 mM, while the concentration of the $NaBH_4$ solution is initially set as 0.588 mM.

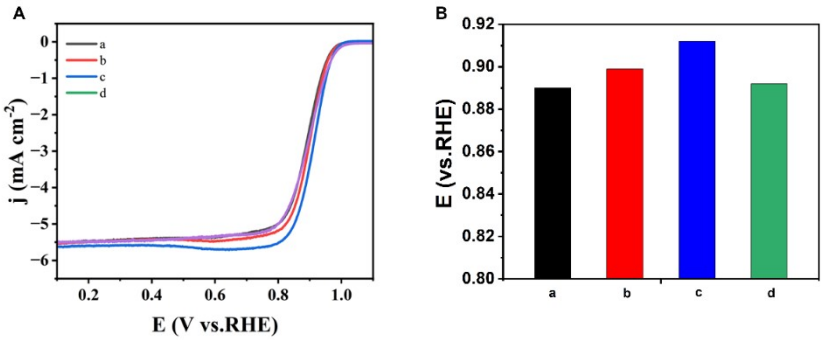

To select the optimal concentration of GSH precursor used for synthesis of S-doped Au@AuPd NWNs with optimal content of S species, four types of S-doped Au@AuPd NWNs were prepared and evaluated by their LSV curves (**Fig. S2A**) and determined by their corresponding $E_{1/2}$ values (**Fig. S2B**). It is clearly seen that the $E_{1/2}$ values of these four types of S-doped Au@AuPd NWNs are 0.890 V, 0.899 V,0.912 V and 0.892 V, respectively. Therefore, the optimal concentration of GSH precursor for synthesis of S-doped Au@AuPd NWNs is 0.120 mM.

Fig. S3 LSV curves (A) and histograms (B) of half-wave potentials ($E_{1/2}$) of five types of S-doped Au@AuPd NWNs (a to e), which were prepared under different concentrations of $NaBH_4$ solution: 0.392 mM (a), 0.490 mM (b), 0.588 mM (c),0.686 mM (d), and 0.784 mM (e). The concentrations of the Pd^{2+} precursor and the GSH precursor are 0.096 mM and 0.120 mM, respectively, and the concentration ratio of Pd^{2+}-to-GSH is determined to be 1:1.25.

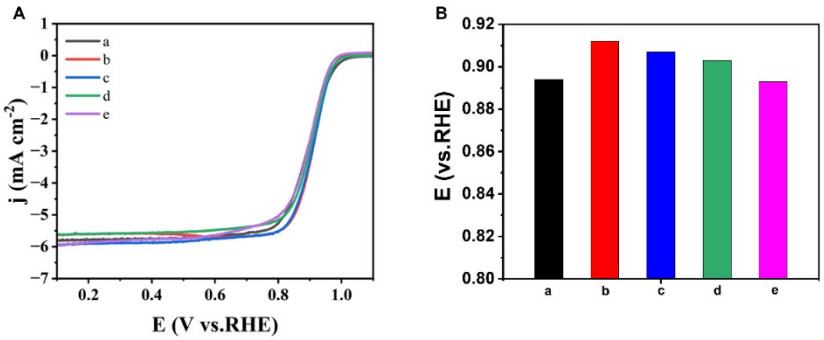

To select the optimal S^{2-}-to-S_2^{2-} radio in the S-doped Au@AuPd NWNs, five types of S-doped Au@AuPd NWNs were prepared and evaluated by their LSV curves (**Fig. S3A**) and determined by their corresponding $E_{1/2}$ values (**Fig. S3B**). It is clearly seen that the $E_{1/2}$ values of these five types of S-doped Au@AuPd NWNs are 0.894 V, 0.912 V, 0.907 V, 0.903 V and 0.892 V, respectively. Therefore, the optimal concentration of $NaBH_4$ solutions used for synthesis of S-doped Au@AuPd NWNs is 0.490 mM at the fixed concentration ratio of Pd^{2+}-to-GSH (1:1.25).

Fig. S4 LSV curves (A) and histograms (B) of half-wave potentials ($E_{1/2}$) of five types of S-doped Au@AuPd NWNs (a to e), which were prepared under different concentrations of Pd^{2+} precursor: 0.098 mM (a), 0.157 mM (b), 0.196 mM (c), 0.392 mM (d), 0.470 mM (e). The concentration of the $NaBH_4$ solution is fixed at 0.490 mM. The concentration of the GSH precursor is adjusted according to that of the Pd^{2+} precursor, while the concentration ratio of Pd^{2+}-to-GSH is maintained at 1:1.25.

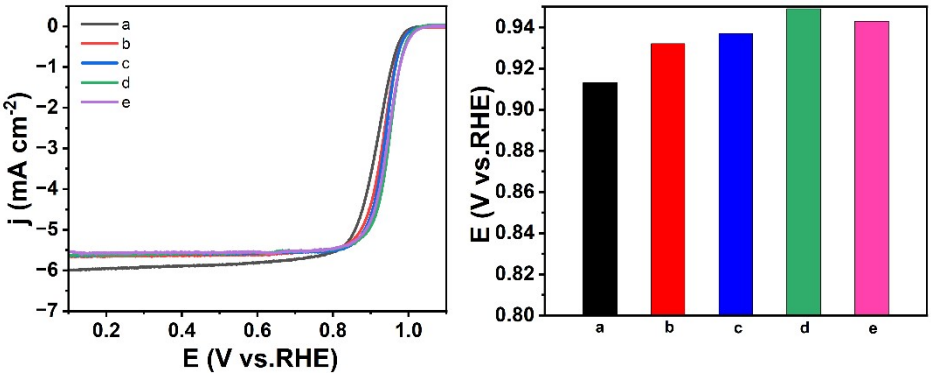

To select the optimal ratio of S^{2-}-to-S_2^{2-} spices in the S-doped Au@AuPd NWNs, five types of S-doped Au@AuPd NWNs were prepared and evaluated by their LSV curves (**Fig. S4A**) and determined by their corresponding $E_{1/2}$ values (**Fig. S4B**). It is clearly seen that the $E_{1/2}$ values of these five types of S-doped Au@AuPd NWNs are 0.913 V, 0.932 V, 0.937 V, 0.949 V and 0.943 V, respectively. Therefore, the optimal concentration of Pd^{2+} precursor used for synthesis of S-doped Au@AuPd NWNs is 0.392 mM at the fixed concentration ratio of Pd^{2+}-to-GSH (1:1.25).

Fig. S5 LSV curves (A) and histograms (B) of half-wave potentials ($E_{1/2}$) of four types of S-doped Au@AuPd NWNs (a to d), which were prepared under different concentrations of GSH precursor: 0.392 mM (a), 0.490 mM (b), 0.592 mM (c), 0.690 mM (d). The concentration of the Pd^{2+} precursor is fixed at 0.392 mM. The concentration of the $NaBH_4$ solution is adjusted according to that of the GSH precursor while the concentration ratio of $NaBH_4$-to-GSH is maintained at 1:1.

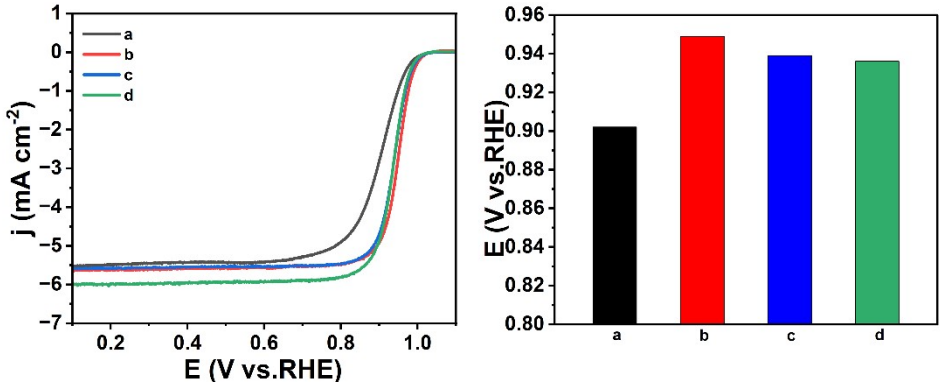

To select the optimal ratio of S^{2-}-to-S_2^{2-} spices in the S-doped Au@AuPd NWNs, four types of S-doped Au@AuPd NWNs were prepared and evaluated by their LSV curves (**Fig. S5A**) and determined by their corresponding $E_{1/2}$ values (**Fig. S5B**). It is clearly seen that the $E_{1/2}$ values of these four types of S-doped Au@AuPd NWNs are 0.902 V, 0.949 V, 0.939 V and 0.936 V, respectively. Therefore, the optimal concentration of GSH precursor used for synthesis of S-doped Au@AuPd NWNs is 0.490 mM at the fixed concentration ratio of $NaBH_4$-to-GSH (1:1).

Fig. S6 LSV curves (A) and histograms (B) of half-wave potentials ($E_{1/2}$) of five types of S-doped Au@AuPd NWNs (a to e), which were prepared under different concentrations of $NaBH_4$: 0.392 mM (a), 0.490 mM (b), 0.588 mM (c), 0.686 mM (d), 0.784mM (e). The concentrations of the Pd^{2+} precursor and the GSH precursor are 0.392 mM and 0.490 mM, respectively, and the concentration ratio of Pd^{2+}-to-GSH is determined to be 1:1.25.

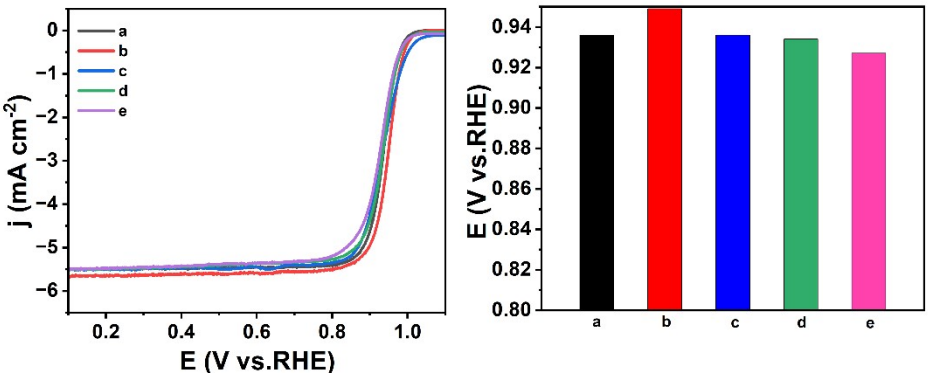

To select the optimal ratio of S^{2-}-to-S_2^{2-} spices in the S-doped Au@AuPd NWNs, five types of S-doped Au@AuPd NWNs were prepared and evaluated by their LSV curves (**Fig. S6A**) and determined by their corresponding $E_{1/2}$ values (**Fig. S6B**). It is clearly seen that the $E_{1/2}$ values of these five types of S-doped Au@AuPd NWNs are 0.936 V, 0.949 V, 0.936 V, 0.934 V and 0.927 V, respectively. Therefore, the optimal concentration of $NaBH_4$ solutions used for synthesis of S-doped Au@AuPd NWNs is 0.490 mM at the fixed concentration ratio of Pd^{2+}-to-GSH (1:25).

Fig. S7 LSV curves (A) and histograms (B) of half-wave potentials ($E_{1/2}$) of five types of S-doped Au@AuPd NWNs (a to e), which were prepared under different concentrations of Pd^{2+} precursor: 0.098 mM (a), 0.157 mM (b), 0.196 mM (c),0.392 mM (d), and 0.588 mM (e). The concentrations of both the GSH precursor and the $NaBH_4$ solution are 0.490 mM.

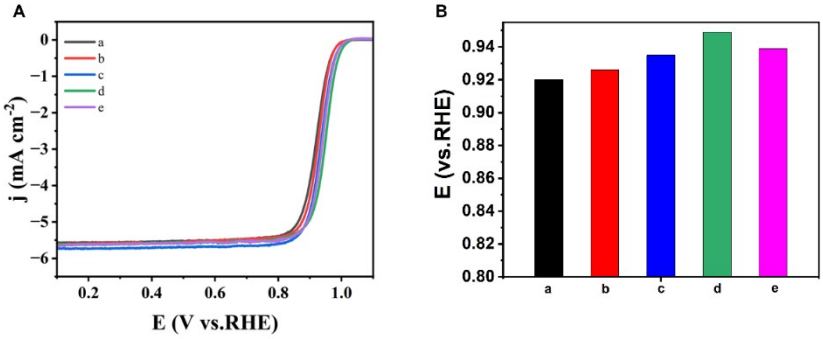

In our previous work, it is found that both S^{2-} and S_2^{2-} species can simultaneously modulate the d-band center of Pd. However, the introduction of S^{2-} and S_2^{2-} species also reduce the ratio of Pd active sites on the outermost surfaces. Therefore, the optimal concentration of Pd^{2+} precursor for the S-doped Au@AuPd NWNs were further investigated at a fixed concentration of GSH precursor. Five types of S-doped Au@AuPd NWNs were prepared and evaluated by their LSV curves (**Fig. S7A**) and determined by their corresponding $E_{1/2}$ values (**Fig. S7B**). It is clearly seen that the $E_{1/2}$ values of five types of S-doped Au@AuPd NWNs are 0.920 V, 0.926 V, 0.935 V, 0.949 V and 0.939 V, respectively. Therefore, the optimal Pd^{2+} concentration for synthesis of S-doped Au@AuPd NWNs is 0.392 mM at a fixed concentration of GSH precursor (0.490 mM).

Fig. S8 HAADF-STEM image of the as-prepared $S_{4.9}$-doped $Au_{89.3}@Au_{1.3}Pd_{5.8}/S^{B3.8A1.1}$ NWNs (a) and their corresponding HAADF-STEM-EDS mapping images of elemental Au (b), Pd (c), and S (d).

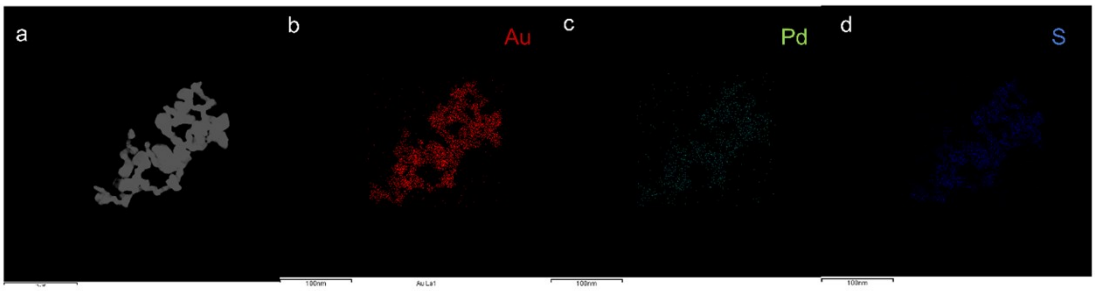

Fig. S9 Energy dispersive X-ray spectroscopy (EDS) spectrum of the as-prepared $S_{4.9}$-doped $Au_{89.3}@Au_{1.3}Pd_{5.8}/S^{B3.8A1.1}$ NWNs.

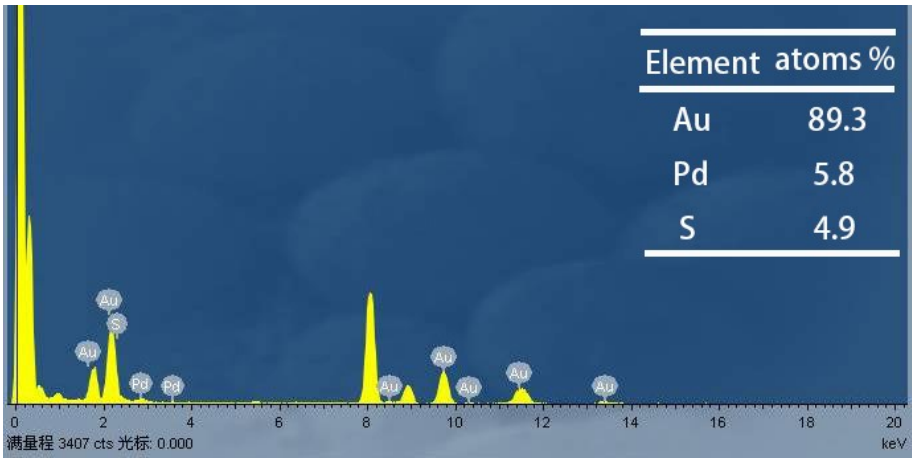

Fig. S10 CO stripping voltammograms of commercial Pd/C catalysts(a), Au@AuPd NWNs (b) and the as-prepared $S_{4.9}$-doped $Au_{89.3}@Au_{1.3}Pd_{5.8}/S^{B3.8A1.1}$ NWNs (c), which were measured in 0.5 M H_2SO_4 solution at a scan rate of 50 mV s^{-1}.

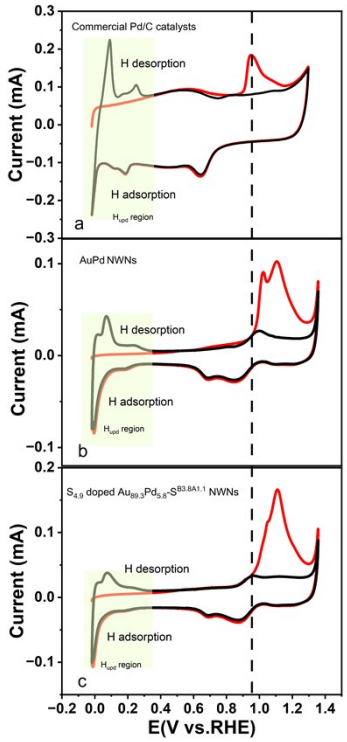

In their CO stripping voltammograms (**Fig. S10**), one can clearly see that the peaks in the H_{upd} region of commercial Pd/C catalysts (**Fig. S10a**) are rather sharp, while those of Au@AuPd NWNs (**Fig. S10b**) become weak and broad. This result indicates that Au@AuPd NWNs still have Pd-rich surfaces (Au-Pd alloyed surfaces). It is well known that pure Pd atoms are also the main H_2 adsorption sites. The H_{upd} region in the as-prepared $S_{4.9}$-doped $Au_{89.3}@Au_{1.3}Pd_{5.8}/S^{B3.8A1.1}$ NWNs with doping of sulfur species (curve c in Fig. S10) becomes weaker and broader. The result indicates a reduction in the number of Pd atoms on the outer surfaces of the as-prepared $S_{4.9}$-doped $Au_{89.3}@Au_{1.3}Pd_{5.8}/S^{B3.8A1.1}$ NWNs. Therefore, some Pd atoms are likely bonded with sulfur species, resulting in a decrease in the number of H_2 adsorption sites.

Fig. S11 CV curves of Au@AuPd NWNs (black curve) and the as-prepared $S_{4.9}$-doped $Au_{89.3}@Au_{1.3}Pd_{5.8}/S^{B3.8A1.1}$ NWNs (red curve), which were measured in O_2-saturated 0.1 M KOH solution.

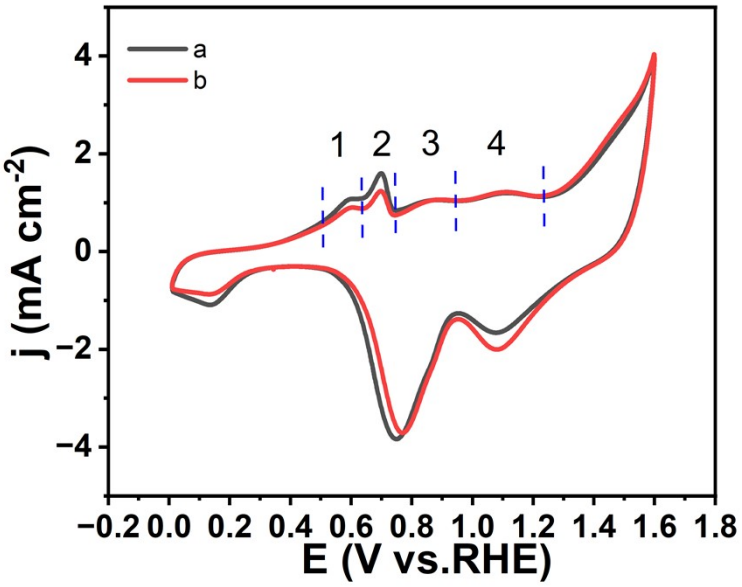

Fig. S12 CV curves of Au@AuPd NWNs (black curve) and $S_{4.9}$-doped $Au_{89.3}@Au_{1.3}Pd_{5.8}/S^{B3.8A1.1}$ NWNs (red curve), which were measured in O_2-saturated 0.1 M KOH solution.

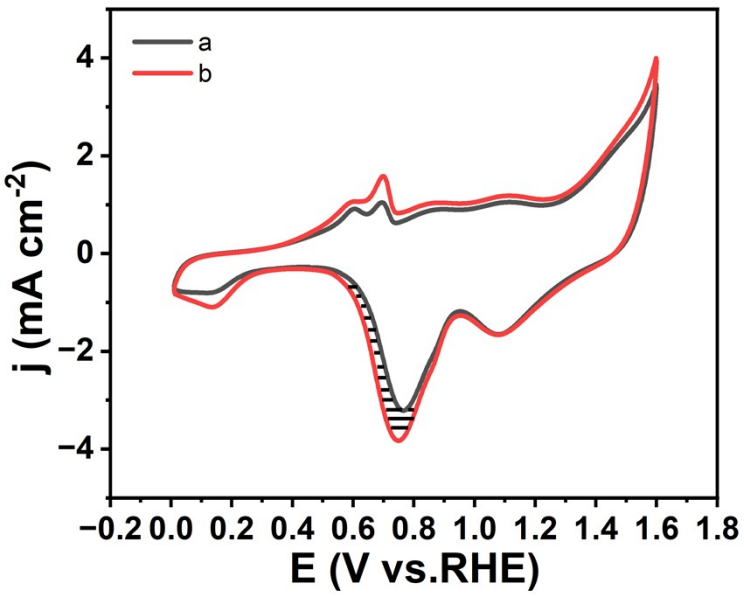

Fig. S13 XRD pattern of Au@AuPd NWNs (black) and the as-prepared $S_{4.9}$-doped $Au_{89.3}@Au_{1.3}Pd_{5.8}/S^{B3.8A1.1}$ NWNs (red). The standard PDF cards of Au (JCPDS no. 04-0784), Pd (JCPDS no. 46-1043), $Pd_{2.8}S$ (JCPDS no. 10-0334) and PdS_2 (JCPDS no. 11-0497) are also shown for better comparison.

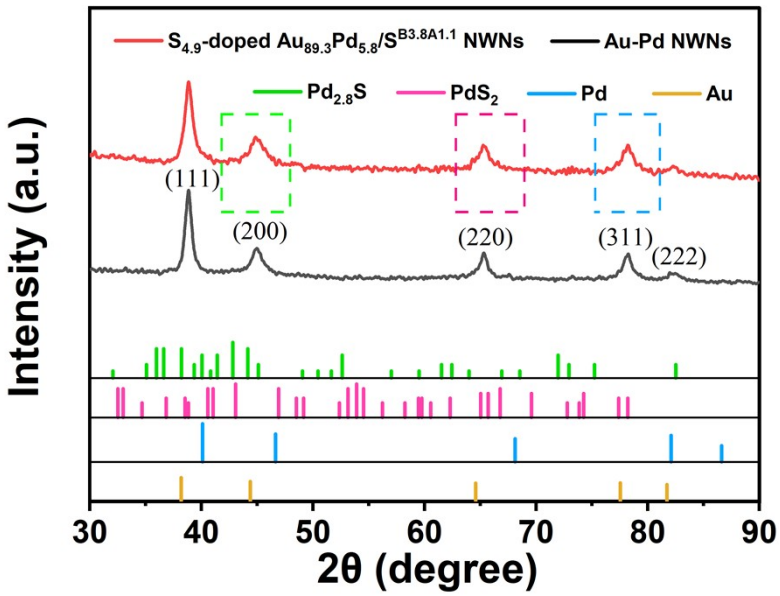

The main compounds that may be existed in the as-prepared $S_{4.9}$-doped $Au_{89.3}@Au_{1.3}Pd_{5.8}/S^{B3.8A1.1}$ NWNs were further determined by XRD. For better comparison and analysis, the XRD patterns of Au@AuPd NWNs were also conducted. As shown in Fig. S10, the main diffraction peaks of the as-prepared $S_{4.9}$-doped $Au_{89.3}@Au_{1.3}Pd_{5.8}/S^{B3.8A1.1}$ NWNs are located around 38.8°, 45.0°, 65.3°, 78.3°and 82.5°, which are attributed to pure Au (JCPDS no. 04–0784) because of the high content of elemental Au as the cores of the resulting $S_{4.9}$-doped $Au_{89.3}@Au_{1.3}Pd_{5.8}/S^{B3.8A1.1}$ NWNs. And the diffraction peak at 82.2°in the XRD pattern of the $S_{4.9}$-doped $Au_{89.3}@Au_{1.3}Pd_{5.8}/S^{B3.8A1.1}$ NWNs can be assigned to Pd (JCPDS no. 46-1043), the results confirm the presence of a quantifiable amount of palladium (Pd) in the sample. However, no other significant palladium diffraction peaks were observed, which should be attributed to the low palladium content.

Moreover, the diffraction of the as-prepared $S_{4.9}$-doped $Au_{89.3}@Au_{1.3}Pd_{5.8}/S^{B3.8A1.1}$ NWNs included in the green (from 41.7° to 48.0°), pink (from 62.6°to 69.2°), and blue (from 75.3°to 81.1°) rectangles are in good agreement with those of the $Pd_{2.8}S$ and PdS_2, according to the corresponding standard PDF cards (JCPDS no. 10–0334 and no. 11–0497), which also have been reported in our previous work. In our previous work[1], the actual content of PdS_2 and $Pd_{2.8}S$ compounds in S-doped AuPd aerogels was slightly higher; thus, smaller shoulder peaks could be observed in the XRD patterns, which can be used to confirm the formation of PdS_2 and $Pd_{2.8}S$ compounds. Since the method used to form PdS_2 and $Pd_{2.8}S$ compounds in S-doped AuPd

nanomaterials is nearly identical, PdS_2 and $Pd_{2.8}S$ compounds should be formed. Although these shoulder peaks are not observed in the XRD patterns, the presence of PdS_2 and $Pd_{2.8}S$ compounds in the sample should impact the corresponding peaks—which also contain the characteristic patterns of PdS_2 and $Pd_{2.8}S$ compounds. Therefore, their presence in the sample is evidenced by analyzing the change in the full width at half maximum (FWHM) of the corresponding peaks—which also contain the characteristic patterns of PdS_2 and $Pd_{2.8}S$ compounds—in the XRD patterns of the samples before and after S doping.

It is worth nothing that through the comparison of XRD full width at half maximum (FWHM) between Au@AuPd NWNs and $S_{4.9}$-doped $Au_{89.3}@Au_{1.3}Pd_{5.8}/S^{B3.8A1.1}$ NWNs (Table S2), the FWHM values of the (1 1 1), (2 0 0), (2 2 0) and (3 1 1) crystalline planes for $S_{4.9}$-doped $Au_{89.3}@Au_{1.3}Pd_{5.8}/S^{B3.8A1.1}$ NWNs are all broader than those of Au@AuPd NWNs. In contrast, the FWHM at the (2 2 2) crystalline plane of $S_{4.9}$-doped $Au_{89.3}@Au_{1.3}Pd_{5.8}/S^{B3.8A1.1}$ NWNs is narrower compared to that of Au@AuPd NWNs at the same (2 2 2) plane. That's because the FWHM broadening of the (1 1 1), (2 0 0), (2 2 0), and (3 1 1) planes in $S_{4.9}$-doped $Au_{89.3}@Au_{1.3}Pd_{5.8}/S^{B3.8A1.1}$ NWNs originates from $NaBH_4$-mediated S-S bond cleavage in GSSG, producing sulfur anionic species (S^{2-}/S_2^{2-}) that strain the Au lattice via Au-S interactions. Conversely, the sharpened (2 2 2) plane reflects PdS_2/ $Pd_{2.8}S$ phase stabilization at Au (2 2 2)-Pd (3 1 1) interfaces, overriding Au-S bonding effects. In brief, Au, PdS_2, $Pd_{2.8}S$ and Pd should exist in the as-prepared $S_{4.9}$-doped $Au_{89.3}@Au_{1.3}Pd_{5.8}/S^{B3.8A1.1}$ NWNs.

Fig. S14 Structural formula of glutathione disulfide (GSSG) molecule.

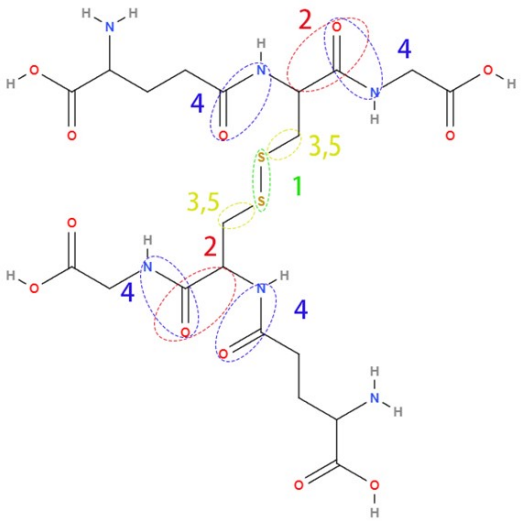

Based on results reported in the literature[2], GSH molecules can react with Au(III) ions remained in the mixture upon their addition. The relevant reaction equation is shown as follows:

$$Au\ (III) + 2GSH \rightarrow Au\ (I) + GS\text{-}SG$$

Fig. S15 XPS spectra of Au 4f signals of pure Au NPs (a), Au@AuPd NWNs (b), and the as-prepared $S_{4.9}$-doped $Au_{89.3}@Au_{1.3}Pd_{5.8}/S^{B3.8A1.1}$ NWNs (c).

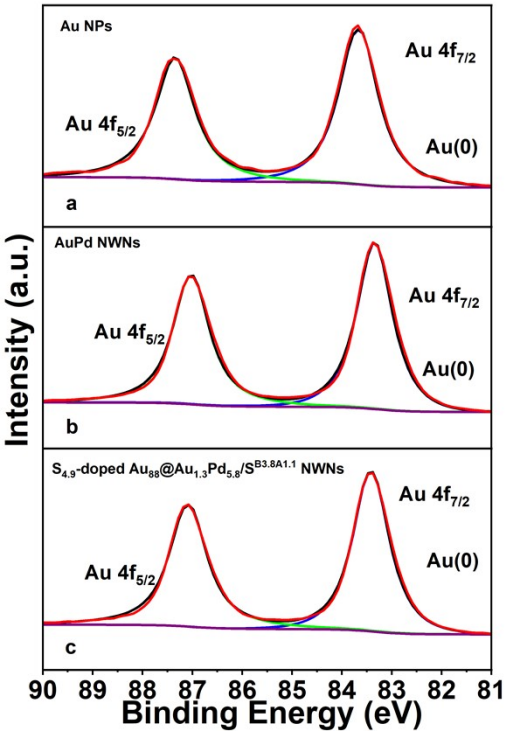

Fig. S16 XPS spectrum of O 1s signals of the as-prepared $S_{4.9}$-doped $Au_{89.3}@Au_{1.3}Pd_{5.8}/S^{B3.8A1.1}$ NWNs.

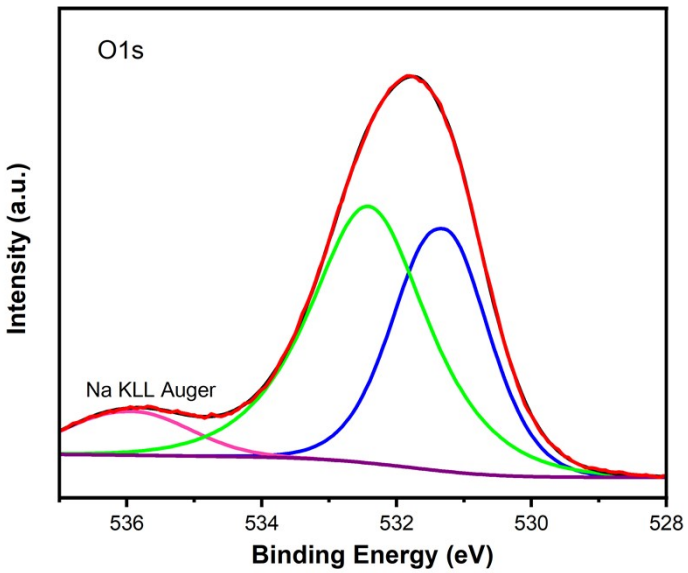

As shown in **Fig. S16**, the peak positions of two main BEs of O 1s signal of the as-prepared $S_{4.9}$-doped $Au_{89.3}@Au_{1.3}Pd_{5.8}/S^{B3.8A1.1}$ NWNs are about 531.3 eV and 532.4 eV, which are ascribed to the surface hydroxyl groups and adsorbed water, respectively, instead of the lattice oxygen.

Fig. S17 Koutecky-Levich (K-L) plots of commercial Pt/C catalysts(a) and the as-prepared $S_{4.9}$-doped $Au_{89.3}@Au_{1.3}Pd_{5.8}/S^{B3.8A1.1}$ NWNs (b) within the potential range from 0.5 to 0.7 V.

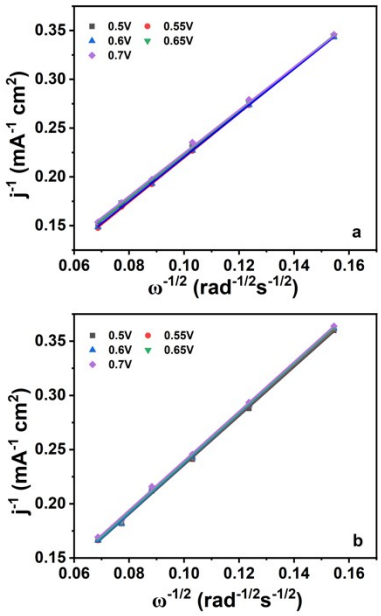

Fig. S18 LSV curves of commercial Pt/C catalysts(a) and the as-prepared $S_{4.9}$-doped $Au_{89.3}@Au_{1.3}Pd_{5.8}/S^{B3.8A1.1}$ NWNs (b), measured in O_2-saturated 0.1 M KOH solution at a scan rate of 10 mV s^{-1} and rotation speeds ranging from 400 to 2025 rpm.

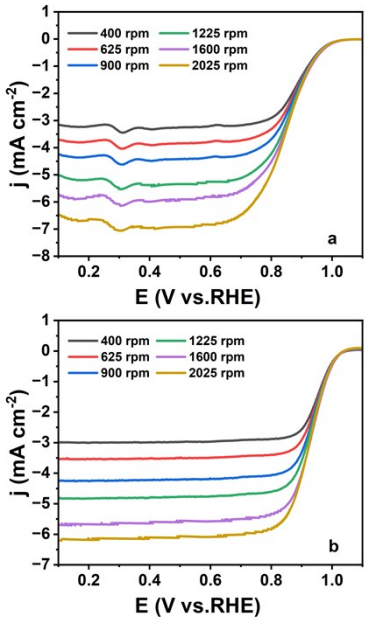

The electron transfer number (n) and kinetic current density (j_k) are obtained from the Koutecky-Levich equation:

$$\frac{1}{j}=\frac{1}{j_k}+\frac{1}{j_d}=\frac{1}{j_k}+\frac{1}{B\omega^{1/2}} \qquad B=0.62nFC_0D_0^{2/3}\nu^{-1/6}$$

where j is the measured current density; j_k is the kinetic current density; j_d is the diffusion-limiting current density; ω is the angular velocity ($\omega=2\pi N$, where N is the rotational speed); n is the electron transfer number in the overall reaction; F is the Faraday constant (96485 C mol^{-1}); C_0 is the bulk concentration of dissolved oxygen (1.2×10^{-6} mol cm^{-3} in 0.1 M KOH solution); D_0 is the diffusion coefficient of dissolved oxygen (1.9×10^{-5} cm^2 s^{-1} in 0.1 M KOH solution); and ν is the kinematic viscosity of the electrolyte (0.01 cm^2 s^{-1} for 0.1 M KOH solution).

Fig. S19 Electron transfer number of the as-prepared $S_{4.9}$-doped $Au_{89.3}@Au_{1.3}Pd_{5.8}/S^{B3.8A1.1}$ NWNs (a) and commercial Pt/C catalysts (b) at different potentials.

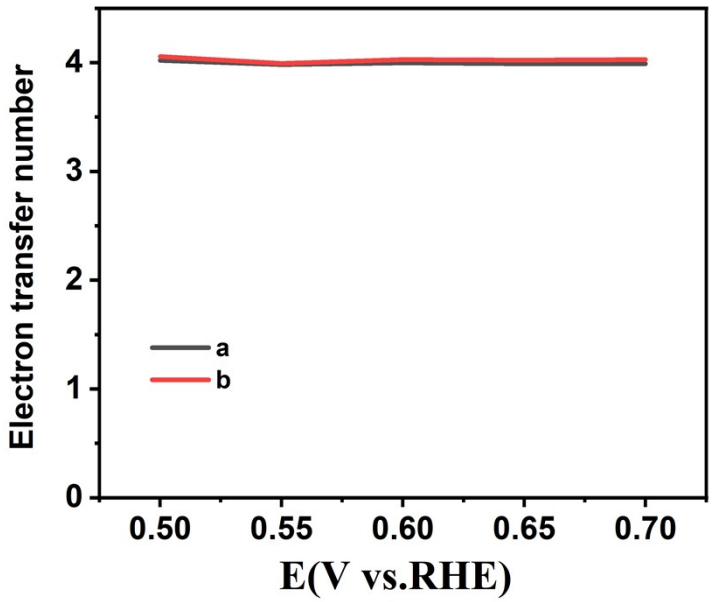

Fig. S20 RRDE polarization curves of the as-prepared $S_{4.9}$-doped $Au_{89.3}@Au_{1.3}Pd_{5.8}/S^{B3.8A1.1}$ NWNs toward the ORR on the Pt disk electrode (b) and for HO_2^- oxidation on Pt ring electrode (a) in O_2-saturated 0.1 M KOH solution. I_{ring} is the ring current and I_{disk} is the disk current.

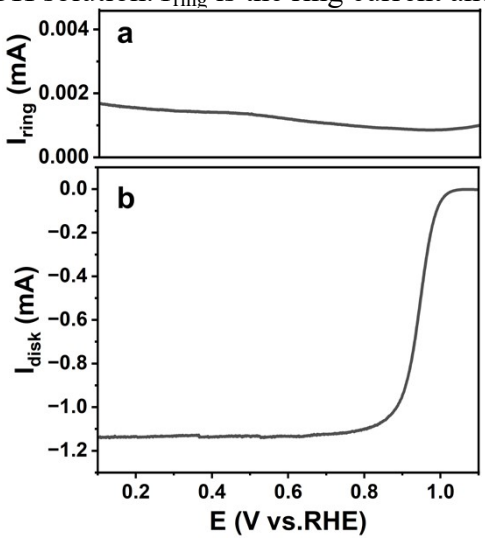

Fig. S20 shows a typical RRDE curves. One can see that the limiting value of the ring current (I_{ring}) due to HO_2^- oxidation is about 1.68 μA, which is rather smaller compared with that (1.12 mA) of the disk current (I_{disk}). The fraction of H_2O_2 produced during the ORR can be estimated by the following equation:

$$H_2O_2\,(\%) = 200 \times \frac{\frac{I_{ring}}{N}}{I_{disk} + \frac{I_{ring}}{N}}$$

where I_{ring} is the ring current, I_{disk} is the disk current, N is the current collection efficiency of the Pt ring electrode (N=0.26).

After calculation, the fraction of H_2O_2 generated at the ring disk during the ORR was estimated to be 1.1%, demonstrating that negligible amounts of H_2O_2 were formed during the ORR.

Fig. S21 EIS spectra of the as-prepared $S_{4.9}$-doped $Au_{89.3}@Au_{1.3}Pd_{5.8}/S^{B3.8A1.1}$ NWNs (a) and the commercial Pt/C catalysts (b).

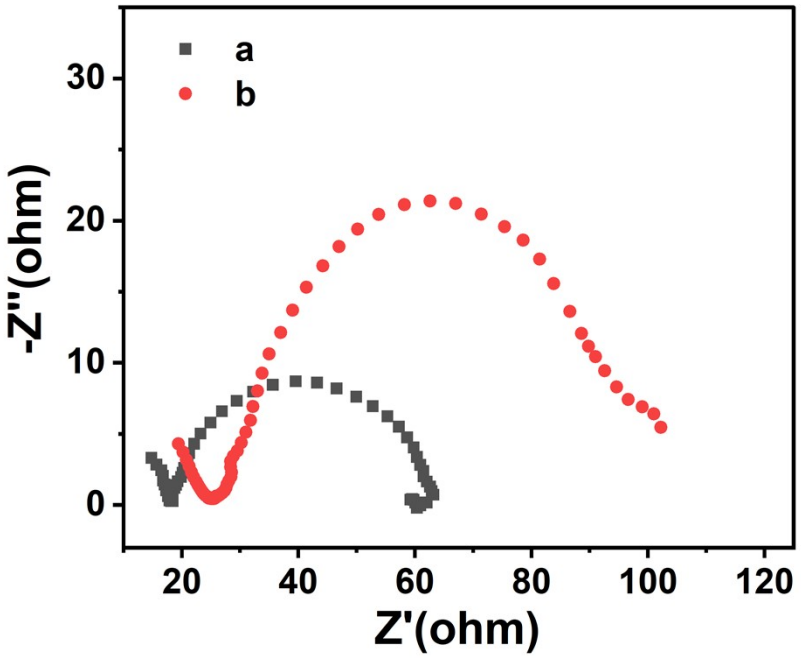

Fig. S22 CO stripping voltammograms of commercial Pt/C catalysts (a) and the as-prepared $S_{4.9}$-doped $Au_{89.3}@Au_{1.3}Pd_{5.8}/S^{B3.8A1.1}$ NWNs (b), measured in 0.5 M H_2SO_4 solution at a scan rate of 50 mV s^{-1}.

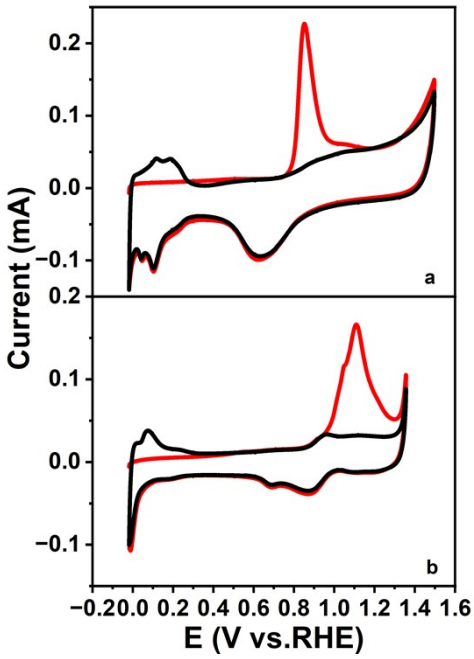

The electrochemical active surface areas (ECSA) of the samples are calculated according to the following equation:

$$ECSA = \frac{Q}{mc}$$

where Q is the charge in the CO adsorption region; m is the mass loading of Pd or Pt on the electrode; and C is the charge required for monolayer adsorption of CO on their surfaces (420 μC cm^{-2} for Pt and Pd).

The ECSA values of commercial Pt/C catalysts and the as-prepared $S_{4.9}$-doped $Au_{89.3}@Au_{1.3}Pd_{5.8}/S^{B3.8A1.1}$ NWNs are calculated to be about 63.1 m^2 g_{pt}^{-1} and 103.8 m^2 g_{pd}^{-1}, respectively. The result indicates that the as-prepared $S_{4.9}$-doped $Au_{89.3}@Au_{1.3}Pd_{5.8}/S^{B3.8A1.1}$ NWNs possess more exposed active sites.

Fig. S23 LSV curves of commercial Pt/C catalysts before and after the ADT of 10k cycles between 0.5 and 0.9 V with a scan rate of 100 mV s^{-1} in the 0.1 M KOH solution.

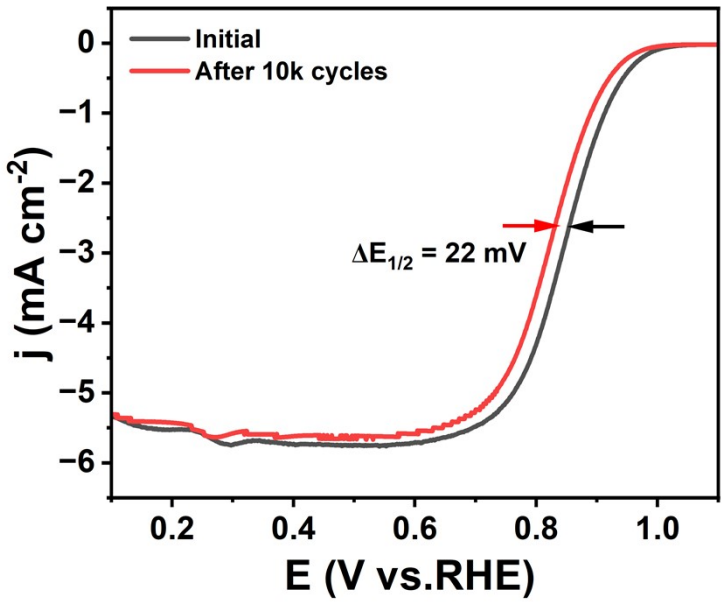

Fig. S24 TEM images of the as-prepared $S_{4.9}$-doped $Au_{89.3}@Au_{1.3}Pd_{5.8}/S^{B3.8A1.1}$ NWNs after the ADT of 10k cycles between 0.5 and 0.9 V with a scan rate of 100 mv s^{-1} in the 0.1 M KOH solution.

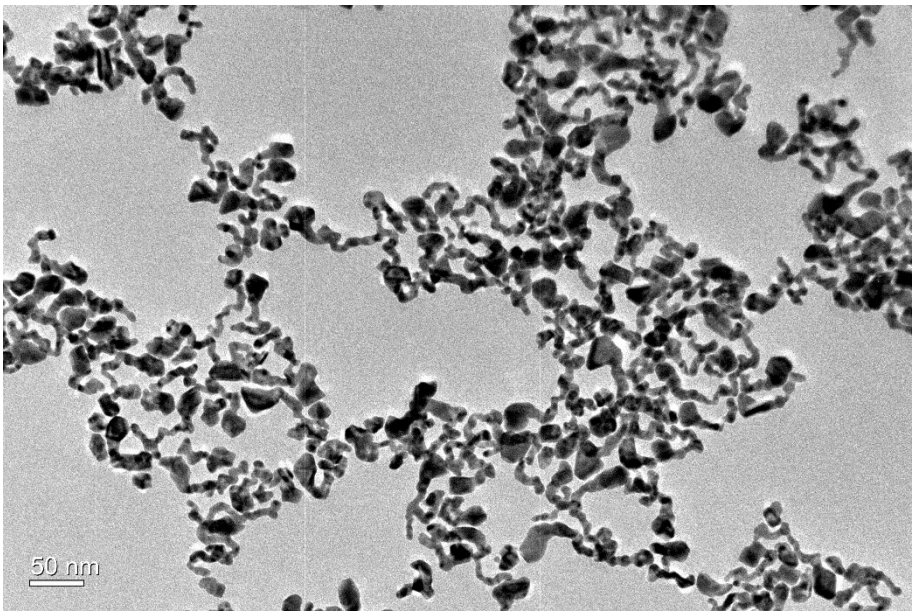

Table S1. Comparison of potential ranges and center positions of the main oxidation peaks in the CV curves of Au@AuPd NWNs and the as-prepared $S_{4.9}$-doped $Au_{89.3}@Au_{1.3}Pd_{5.8}/S^{B3.8A1.1}$ NWNs, measured in N_2-saturated 0.1 M KOH solution. W and S represent that the peak intensities are weak and strong, respectively.

Sample	Peak 1		Peak 2		Peak 3		Peak 4	
	Potential range (V)	**Center position (V)**	**Potential range (V)**	**Center position (V)**	**Potential range (V)**	**Center position (V)**	**Potential range (V)**	**Center position (V)**
Pd {1 1 0}	-	-	-	-	0.75 - 0.90	0.88	-	-
Pd {1 1 1}	0.63 - 0.75 (W)	0.70 (W)	0.75 - 0.85 (W)	0.80 (W)	-	-	0.95 - 1.17 (S)	1.08 (S)
Pd {1 0 0}	-	-	-	-	0.72 - 0.83 (W) 0.83 - 0.92 (S)	0.80 (W) 0.90 (S)	-	-
Au@AuPd NWNs	0.52 - 0.65	0.60	0.65 - 0.75	0.70	0.75 - 0.97	0.90	0.97 - 1.25	1.07
Our sample	0.52 - 0.65	0.60	0.65 - 0.75	0.70	0.75 - 0.97	0.90	0.97 - 1.25	1.07

Table S2. Comparison of FWHM values of the main peaks in XRD patterns of Au@AuPd NWNs and the as-prepared $S_{4.9}$-doped $Au_{89.3}@Au_{1.3}Pd_{5.8}/S^{B3.8A1.1}$ NWNs.

FWHM values	Au@AuPd NWNs	Our Sample
(1 1 1)	0.73	1.03
(2 0 0)	1.26	2.14
(2 2 0)	1.13	1.37
(3 1 1)	1.23	1.42
$(2\ 2\ 2)_{Au}/(3\ 1\ 1)_{Pd}$	1.27	0.72

Table S3. Summarized data of the center positions of the main peaks in the Raman spectra of GSH and GSSG molecules, where *v* and *∂* represent stretching vibration and in-plane bending vibration, respectively.

Peak number	Raman Shift(cm^{-1})	Assignment
1	513	$_{\nu}$(S-S)
2	623	$_{\delta}$(CCO)
3	663	$_{\nu}$(CS)
4	678	$_{\delta}$(OCN)
5	726	$_{\nu}$(CS)

Table S4. Comparison of electrocatalytic performance toward the ORR in 0.1 M KOH solutions between the as-prepared $S_{4.9}$-doped $Au_{89.3}@Au_{1.3}Pd_{5.8}/S^{B3.8A1.1}$ NWNs and other Pd-based electrocatalysts reported in the literature.

Sample	$E_{1/2}$ [V]	$E_{1/2}$ of Pt/C [V]	$\Delta E_{1/2}$ [mV]	$\Delta Pd3d_{5/2}$ [eV]	Reference
$S_{4.9}$-doped $Au_{89.3}@Au_{1.3}Pd_{5.8}/S^{B3.8A1.1}$ NWNs	**0.949**	**0.855**	**94**	**+0.40**	**This work**
AuPd–$SB_{67}A_{33}$ aerogels	0.970	0.885	85	+0.40	*J. Mater. Chem. A*, 2022, 10, 7800–7810.
$Au_{81}Pd_2Pt_9$-$S_8^{B4.6A3.4}$ aerogels	0.961	-	94	+0.43	*Chem. Eng. J.*, 2023, 470: 144149.
Au-Pd NW_{60}	0.918	0.873	45	+0.41	*Small*, 2022, 18(44): 2203458.
Ag@PdNi NCs	0.913	0.893	20	-2.70	*Chem. Eng. J.*, 2024, 500: 156765.
PdZnBi/NC-IR	0.895	0.865	30	-0.2	*J. Mater. Chem. A*, 2024,12, 8194-8204
PdZn/TiO_{2-x} NS	0.834	-	-	+2.0	*J. Mater. Chem. A*, 2022,10, 13987-13997
COF@ZIF-Pd_{800}	0.866	0.822	44	+0.7	*Small*, 2024: 2403655.
PdNC/Pd-NC_{800}	0.850	0.860	-10	+0.02	*Small*, 2024, 20(9): 2307110
Pd-Ni-P MGNP	0.840	-	-	+0.9	*Small*, 2023, 19(33): 2300721.
PdCu nanosheet	0.860	-	-	+0.41	*Small Methods*, 2023, 7(7): 2300021.
Fe&Pd-C/N	0.913	0.846	67	-	*Small*, 2023, 19(38): 2303321.
$Pd_3CuFe_{0.5}$	0.920	-	-	+0.40	*Small*, 2024, 20(19): 2307243
$Pd_{20}ZnS_{10}$ AHSs	0.940	0.877	63	+0.93	*Small*, 2023, 19(50): 2304984.
P-PdMo	0.880	0.850	20	+0.40	*Chem. Eng. J.*, 2024, 486: 150258.
Pd@CS/CNF800	0.917	0.867	50	-	*J. Mater. Chem. A*, 2024,12, 31467-31479
P-PdPb NFs	0.950	0.910	40	+0.73	*J. Mater. Chem. A*, 2022,10, 15528-15534

Reference

1. X. Zhang, J. Wang, M. Zhang, X. Yue, W. Du, W. Fan and H. Xia, *J. Mater. Chem. A*, 2022, **10**, 7800–7810.
2. I. V. Mironov and V. Y. Kharlamova, *Chem. Sel.*, 2023, **8(26)**, e202301337.